

Radial profiles of Fe abundance in the intracluster medium of nearby clusters observed with XMM-Newton

Kyoko Matsushita

Department of Physics, Tokyo University of Science, 1-3 Kagurazaka, Shinjyuku-ku, Tokyo, 162-8601, Japan
e-mail: matusita@rs.kagu.tus.ac.jp

ABSTRACT

Aims. The abundances of Fe in the intracluster medium of nearby ($z < 0.08$) clusters were measured up to $0.3 \sim 0.5r_{180}$.
Methods. We analyzed 28 clusters of galaxies observed with XMM-Newton. We derived Fe abundances from the flux ratios of Fe lines to the continuum within an energy range of 3.5–6 keV to minimize and evaluate systematic uncertainties.

Results. The radial profiles of the Fe abundances of relaxed clusters with a cD galaxy at their X-ray peak have similar slopes. These clusters show similar enhancements in the Fe abundance within $0.1r_{180}$, and at $0.1\text{--}0.3r_{180}$, they have flatter Fe abundance profiles at $0.4\text{--}0.5$ solar, with a small scatter. Most other clusters, including merging clusters, also have similar Fe abundance profiles beyond $0.1r_{180}$. These clusters may have universal metal enrichment histories, and a significant amount of Fe was synthesized at a very early stage in cluster formation. Mergers of clusters can destroy the central Fe peak.

Key words. galaxies:clusters — X-rays:ICM — galaxies:ISM

1. Introduction

Clusters of galaxies are the largest gravitationally bound objects in the universe. The intracluster medium (ICM) contains a large amount of metals, which are synthesized mainly by supernovae (SNe) in early-type galaxies (e.g., Arnaud et al. 1992; Renzini et al. 1993). Thus, metal abundances in the ICM provide important clues for understanding the metal-enrichment history and evolution of galaxies in clusters. Because both SN II and SN Ia synthesize Fe, the distribution of Fe in the ICM contains information about the star-formation histories of massive stars and the history of chemical-enrichment attributed to SN Ia.

The ASCA satellite (Tanaka et al. 1994) first enabled us to measure the distribution of Fe in the ICM (e.g., Fukazawa et al. 2000; Finoguenov et al. 2000; 2001). The Fe abundances of these clusters are $0.2\text{--}0.3$ solar, adopting the solar abundance from the “photospheric” values given by Anders and Grevesse (1989). The dependence of the Fe abundance on the temperature of the ICM is weak (Fukazawa et al. 1998). ASCA revealed large-scale abundance gradients from AWM 7 and the Perseus cluster (Ezawa et al. 1997; 2001). De Grandi et al. (2004) derived the Fe abundances of nearby hot clusters observed with Beppo-SAX and found that the abundance profiles are strongly peaked for cool core clusters, whereas they remain constant for other systems. XMM-Newton and Chandra observations show a spatial distribution of the Fe abundance of up to $0.3 \sim 0.4r_{180}$ (e.g., Tamura et al. 2004; Vikhlinin et al. 2005; Baldi et al. 2007; Maughan et al. 2008; Leccardi & Molendi 2008). At the center of most relaxed clusters, the Fe abundance decreases steeply outward. Outside the

central region, the Fe abundance decreases more gradually toward the outer regions.

The Suzaku satellite first measured the Fe abundance of the ICM beyond $0.5r_{180}$. (Fujita et al. 2008; Tawa 2008). Within $0.3\text{--}0.5r_{180}$, Suzaku can derive the Fe abundances more accurately than XMM. The Fe abundance gradually decreases from the center to $\sim 0.7r_{180}$.

In this paper, we describe our study of the Fe abundance in the ICM up to $0.3 \sim 0.5r_{180}$ of 28 brightest clusters of galaxies observed with XMM-Newton. Some clusters have cool cores at their center (e.g. Makishima et al. 2001; Böhringer et al. 2002). We must be careful when deriving elemental abundances with a multi-temperature plasma, because emission lines and a continuum spectrum are different functions of temperature. Therefore, we directly derived the strength of the $K\alpha$ lines of Fe, considering the temperature dependence of the flux ratios of the Fe lines and the continuum, and derived Fe abundances. We adopted an energy range in which the ICM dominates the background.

In Section 2 we summarize the observations and data preparation. Section 3 describes our analysis of the data, and in Section 4 the Fe abundances are determined. We discuss our results in Section 5.

We adopt the new solar abundances given by Lodders (2003), according to which the solar Fe abundance with regard to H is 2.95×10^{-5} by number. This value differs from the photospheric value (4.68×10^{-5}) given by Anders and Grevesse (1989). Considering the difference in He abundance between the two solar abundance tables, the Fe abundance yielded by the former is 1.5 times higher than that of the latter. We use $H_0 = 70$ km/s/Mpc. Unless otherwise specified, errors are quoted with 68% confidence.

2. Target selection and observations

In the XMM-Newton archival data, we selected the 28 brightest clusters of galaxies with $z < 0.08$ and total exposures above 7 ks after filtering out background flares. The samples are listed in Table 1. The ICM temperatures in the “the X-ray Brightest Abell Clusters (XBACs)” by Ebeling et al. (1996) range from 2.4 keV to 8.7 keV. Seventeen clusters show relatively relaxed morphologies with a cD galaxy at the X-ray peak. Hereafter, these are called cD clusters. Eleven clusters are merging clusters or relaxed clusters with two giant galaxies in the central region such as the Coma cluster. Hereafter, these clusters are called non-cD clusters.

The virial radius of each cluster, $r_{180} = 1.95 h_{100}^{-1} \sqrt{k < T > / 10 \text{ keV}}$, was calculated following Markevitch et al. (1998), by adopting an average temperature $< T >$ of that at $0.06\text{--}0.3r_{180}$ from the X-ray peak of each cluster.

We used the PN, MOS1, and MOS2 detectors to derive the Fe abundance of the ICM. We selected events with patterns smaller than 5 and 13 for the PN and MOS, respectively.

Spectra were accumulated in concentric annular regions of $0\text{--}0.03r_{180}$, $0.03\text{--}0.06r_{180}$, $0.06\text{--}0.1r_{180}$, $0.1\text{--}0.2r_{180}$, $0.2\text{--}0.3r_{180}$, and $0.3\text{--}0.5r_{180}$ centered on the X-ray peak of each cluster. Here, the X-ray peaks were derived using the wavelet tool of SAS-v8.0.0, and luminous point sources were excluded. The calculated X-ray peak of each cluster and the accumulation regions for the spectra are summarized as X-ray images in Figure 1. The spectra from MOS1 and MOS2 were added. The background spectrum was calculated by integrating blank-sky data in the same detector regions. From deep-sky observations with the XMM, we selected the data with the background most similar to that of each cluster, and the faintest Galactic emission, after screening out background flare events in the data and the background, following Katayama et al. (2004). Then, the background was scaled using the count rate between 10 and 12 keV. Most scaling factors are smaller than 10%, because we selected a blank-sky observation to match each cluster observation.

The response matrix file and the auxiliary response file (ARF) corresponding to each spectrum were calculated using SAS-v8.0.0. We used the XSPEC_v11.3.2ag package for our spectral analysis.

3. Analysis

3.1. Fe line strength

In this study, the Fe abundances of the ICM are derived from the ratio of the flux in units of photons $\cdot \text{cm}^{-2} \text{s}^{-1}$ of the $K\alpha$ lines of He-like Fe (hereafter F_{FeHeK}) or H-like Fe (hereafter F_{FeHK}) to that of the continuum at 3.5–6.0 keV (hereafter $F_{3.5-6}$), since the systematic uncertainty in the continuum flux in this energy band owing to the background is smaller than that around the Fe-K lines. Another advantage is that the dependence of the ratios on the plasma temperature is relatively weak within a certain temperature range. The temperature dependence of these ratios can constrain on the Fe abundances of multi-temperature plasmas.

To obtain suitable statistics, we simultaneously fitted the raw annular spectra of a cluster and a deep field within an energy range of 5.0–7.2 keV with the sum of the ICM and

background emission. The ICM component consists of thermal bremsstrahlung and two Gaussians for the $K\alpha$ lines of He-like and H-like Fe. We modeled the background emission with a power-law model for the cosmic X-ray background (CXB), a “powerlaw/b” model for non X-ray background (NXB), and three Gaussians at 5.4 keV, 5.9 keV, and 6.4 keV, which are the $K\alpha$ lines of neutral Cr, Mn, and Fe, respectively. The “powerlaw/b” model is not folded through the ARF, and differs from a power-law. We obtained acceptable fits with a reduced $\chi^2 \sim 1$. Figure 2 shows representative spectra of Abell 426 (A426, the Perseus cluster) fitted in this way. These spectra are fitted well, and the $K\alpha$ line of He-like Fe is clearly detected even at $0.3\text{--}0.5r_{180}$. The background line at 6.4 keV may cause a systematic uncertainty in the strength of the He-like Fe line in the MOS spectra at low-brightness regions. In contrast, the background lines in the PN spectra in this energy range are much weaker than those in the MOS.

Despite the 6.4 keV background line, the PN and MOS gave mostly consistent ratios of $F_{\text{FeHeK}}/F_{3.5-6}$ and $F_{\text{FeHK}}/F_{3.5-6}$. Hereafter we used the weighted average of these ratios from the PN and MOS to derive Fe abundances with relative errors smaller than 30%.

3.2. Spectral fit with single-temperature model

To convert the observed line flux to the Fe abundance, we derived the ICM temperatures. The first step in this analysis was to fit the background-subtracted annular (projected) spectra from the PN and MOS with a single-temperature vAPEC model (Smith et al. 2001) with photoelectric absorption fixed at the Galactic value (hereafter the 1T model). The energy ranges of 1.4–1.6 keV for the MOS and 7.2–9.0 keV for the PN were discarded owing to strong instrumental lines. To account for the remaining background, we added a “powerlaw/b” model (Zhang et al. 2009) and fitted the spectra within the energy range of 1.2–10.0 keV. Here, we fixed the photon index of the “powerlaw/b” component at 0.15 and 0.35 for the MOS and PN, respectively (Zhang et al. 2009). The abundances of C, N, and Al were fixed at 1 solar and those of O and Ne were assumed to have the same values as Mg. The abundances of Mg, Si, S, Ar, Ca, Fe, and Ni were allowed to vary. We did not use a more detailed modeling of the background (Snowden et al. 2008; Leccardi & Molendi 2008), since we mainly used an energy range over which the ICM emission is dominant. The ICM temperatures derived from the PN and MOS are consistent with each other within the order of several percent. We adopted the weighted average of the temperatures derived from the PN and MOS, as summarized in Table 2.

To derive the Fe abundance in each annular region, we included a 10% systematic uncertainty in temperatures, considering the uncertainties described below. When the spectra are fitted within the energy range of 0.8–10.0 keV, which includes Fe-L emission, the derived temperatures decreased systematically by $\sim 10\%$. We also fitted the spectra without the “powerlaw/b” model. Then, outside $0.2r_{180}$, the derived ICM temperature increased by 10–20% and the discrepancy between the PN and MOS became increased. Similarly, we also analyzed the same XMM data in the same way with SAS v7.0.0. In this case, when the derived temperatures are higher than several keV, the MOS systematically gives $\sim 10\%$ higher than those given by the

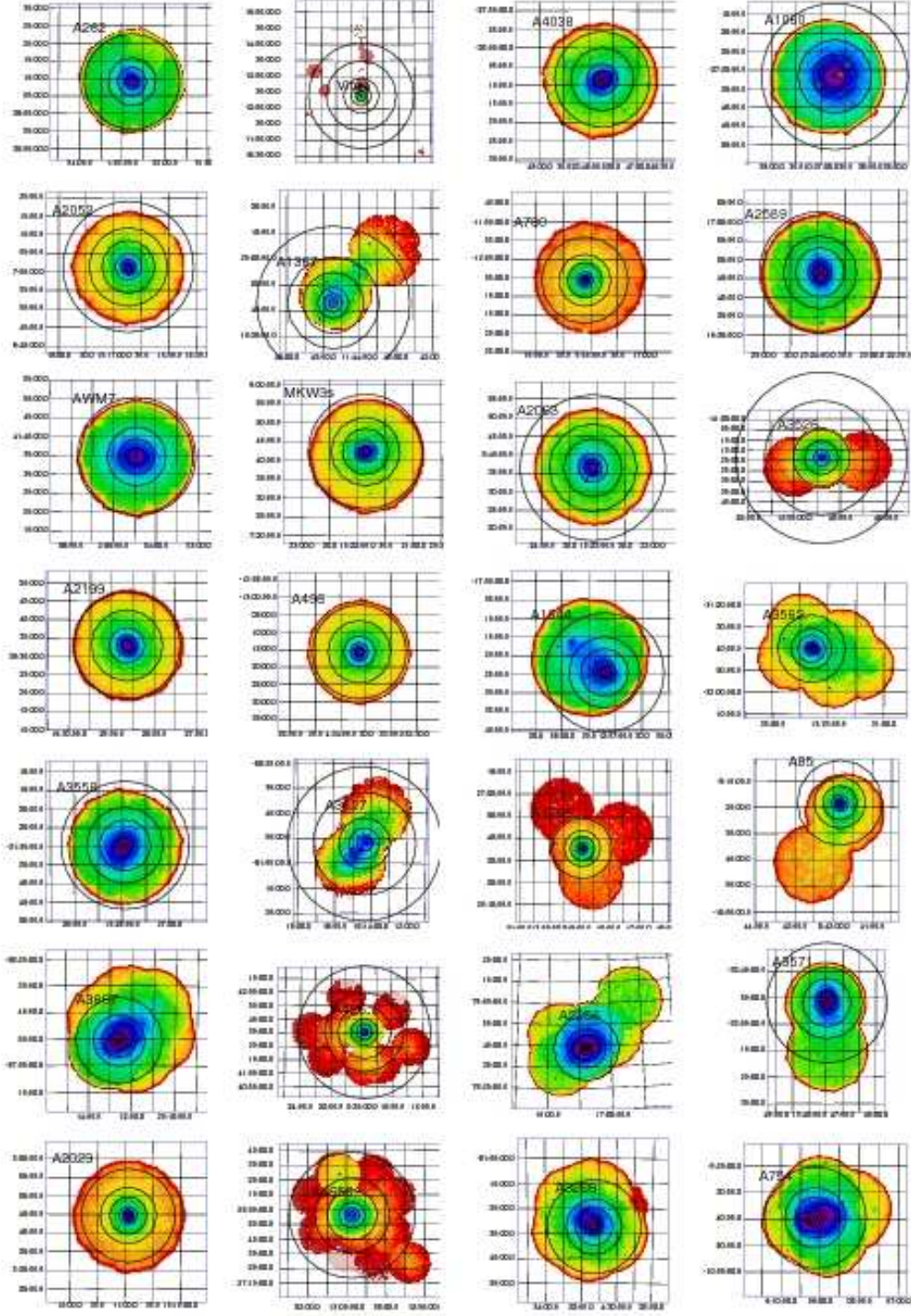


Fig. 1. Combined MOS and PN images of the target clusters. Exposures are not corrected and therefore the exposures of each field can be visualized. Circles have radii of 0.03, 0.06, 0.1, 0.2, 0.3, and $0.5r_{180}$.

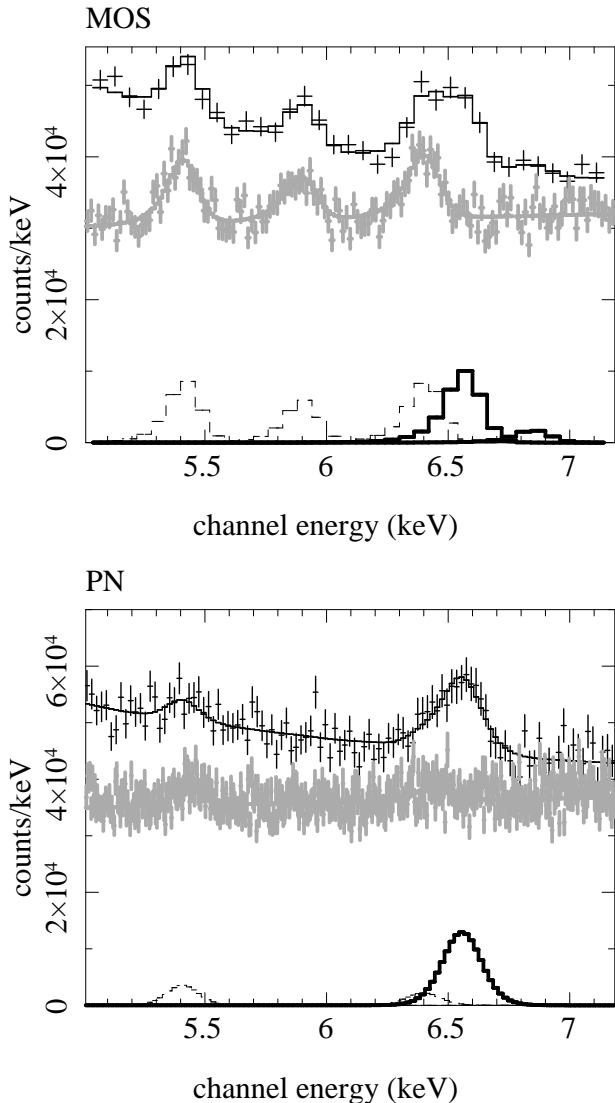


Fig. 2. Representative spectra of Abell 426 (the Perseus cluster) (black) and the adopted background (gray) at $0.3\text{--}0.5r_{180}$ from MOS and PN fitted with Gaussians and continuum. Best-fit Gaussians corresponding to the $K\alpha$ -lines of He-like and H-like Fe are plotted as bold lines: those for background lines are plotted as thin dashed lines.

PN. Systematic differences of $\sim 10\%$ in cluster temperature among Chandra, the PN, and the MOS were reported in relatively high-temperature clusters (Snowden et al. 2008). Reese et al. (2010) found that the ICM temperature derived from Chandra data changes systematically by $\sim 10\%$ between calibrations.

3.3. Spectral fit with multi-temperature model

To study the effect of the temperature structure of the ICM, we also fitted the background-subtracted spectra of the MOS at $0.5\text{--}10.0$ keV, using a multi-temperature vAPEC model with photoelectric absorption (multi-T model), the Galactic emission, and the “powerlaw/b” model with a fixed photon index, as described in Section 3.2. The Galactic emission, which includes the local hot bubble, the Milky Way halo, and solar wind charge exchange, is em-

pirically fitted with a two-temperature APEC model with redshift = 0 (e.g. Lumb et al. 2002; Yoshino et al. 2009). Therefore, we used the two-temperature APEC model for the Galactic emission. The temperature of the one component was fixed at 0.1 keV, and that of the other was restricted within $0.2\text{--}0.4$ keV. Here, we used only the MOS detector, because it has a better energy resolution and is more sensitive to temperature structure than the PN detector. The multi-T model is a sum of 13 temperature components, because the spectrum of an isothermal plasma can be reproduced well by the sum of the spectra of two neighboring temperature plasmas with similar elemental abundances. The ratio of the temperatures of the two neighboring components is fixed at 0.8 . The hottest temperature of the multi-T model is fixed at the highest temperature derived using the 1T model derived from the MOS within $0.2r_{180}$. The elemental abundances of each element for the multi-T components are assumed to have the same values. We added a 3% systematic error to the count rate of each channel in the spectra. Then, the reduced χ^2 reaches the reasonable values of ~ 1 .

4. Results

4.1. Temperature profiles of the ICM

The radial temperature profiles of the ICM are summarized in Figure 3. From $0.06r_{180}$ to $0.2\text{--}0.3r_{180}$, the temperature gradient of the ICM is flat, whereas the temperatures of several cD clusters are lower within $0.06r_{180}$ than those at $0.06\text{--}0.2r_{180}$, owing to the presence of cool cores. In contrast, most non-cD clusters have flatter radial temperature profiles within $0.2\text{--}0.3r_{180}$. Beyond $0.2\text{--}0.3r_{180}$, the ICM temperatures tend to decrease outward. These temperature profiles are consistent with previous Chandra and XMM-Newton measurements (e.g., Snowden et al. 2008; Vikhlinin et al. 2005).

4.2. Fe abundance of the ICM

Figure 4 shows the observed values of $F_{\text{FeHeK}}/F_{3.5-6}$ and $F_{\text{FeHK}}/F_{3.5-6}$, plotted against the ICM temperature derived from the 1T model. Within $0.03r_{180}$, $F_{\text{FeHeK}}/F_{3.5-6}$ is scattered from 0.03 to 0.2 , with mild temperature dependence. Beyond $0.03r_{180}$, both $F_{\text{FeHeK}}/F_{3.5-6}$ and $F_{\text{FeHK}}/F_{3.5-6}$ become closer to the theoretical relationships predicted by the APEC model assuming that the Fe abundance = 0.5 solar. Beyond $0.3r_{180}$, the data for only several clusters have adequate statistics: the $F_{\text{FeHeK}}/F_{3.5-6}$ values of A426 (the Perseus cluster) and a non-cD cluster are close to the relationship for 0.5 solar, whereas those of two non-cD clusters are significantly lower.

The temperature dependence of the theoretical ratio $F_{\text{FeHeK}}/F_{3.5-6}$ for a given Fe abundance is fairly weak, within 20% for $2\text{--}6$ keV, and starts to decrease above 6 keV (Figure 4). In contrast, the ratio of $F_{\text{FeHK}}/F_{3.5-6}$ is nearly constant within 20% for $6.7\text{--}17$ keV. This temperature independence minimizes the systematic uncertainty in the Fe abundance because of uncertainties in the temperature structure.

To derive the Fe abundance, we converted the observed ratio of $F_{\text{FeHeK}}/F_{3.5-6}$ using the theoretical ratios calculated by the APEC model and the ICM temperature de-

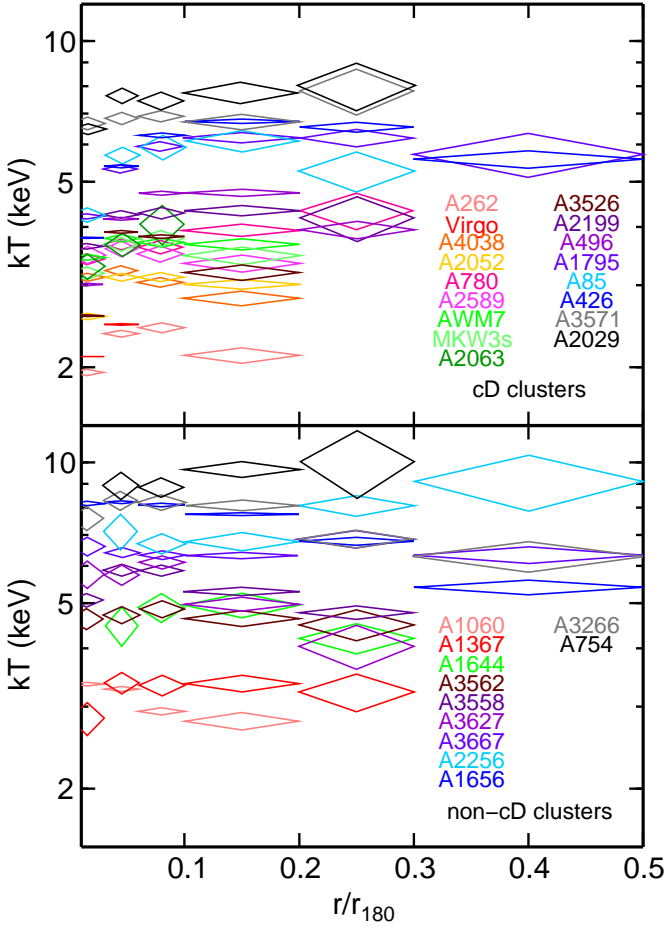


Fig. 3. Radial profiles of the ICM temperature of cD clusters (upper panel) and non-cD clusters (lower panel).

rived from the 1T model. The results are summarized in Table 2.

4.3. Radial profiles of Fe abundances

The radial profiles of the Fe abundances in the ICM are shown in Figure 5. Within $0.03r_{180}$, the derived Fe abundances of the cD clusters are 0.7–1.6 solar. Non-cD clusters with large deviations from spherical symmetry, A1367 and A3562, also have high Fe abundances of ~ 1.5 solar. In contrast, the other non-cD clusters have lower central values of Fe. Outside $0.1r_{180}$, both the cD and non-cD clusters have similar radial profiles of the Fe abundance. At $0.1\text{--}0.2r_{180}$, the derived Fe abundances are ~ 0.5 solar. For the region at $0.3\text{--}0.5r_{180}$, although sufficient statistics are available for only six clusters, the derived Fe abundances are around 0.3–0.5 solar.

Figure 6 shows the ratios of the Fe abundances of each cluster at each annular region to that at $0.06\text{--}0.1r_{180}$. Except for the Centaurus cluster (A3526), the Fe abundances of the cD clusters have similar slopes: the Fe abundances within $0.03r_{180}$ are higher than those at $0.06\text{--}0.1r_{180}$ by a factor of 1.5. Beyond $0.06r_{180}$, the radial profiles become flatter.

The Fe abundances of three morphologically distorted clusters, A1367, A3558, and A3562, within $0.03r_{180}$ are

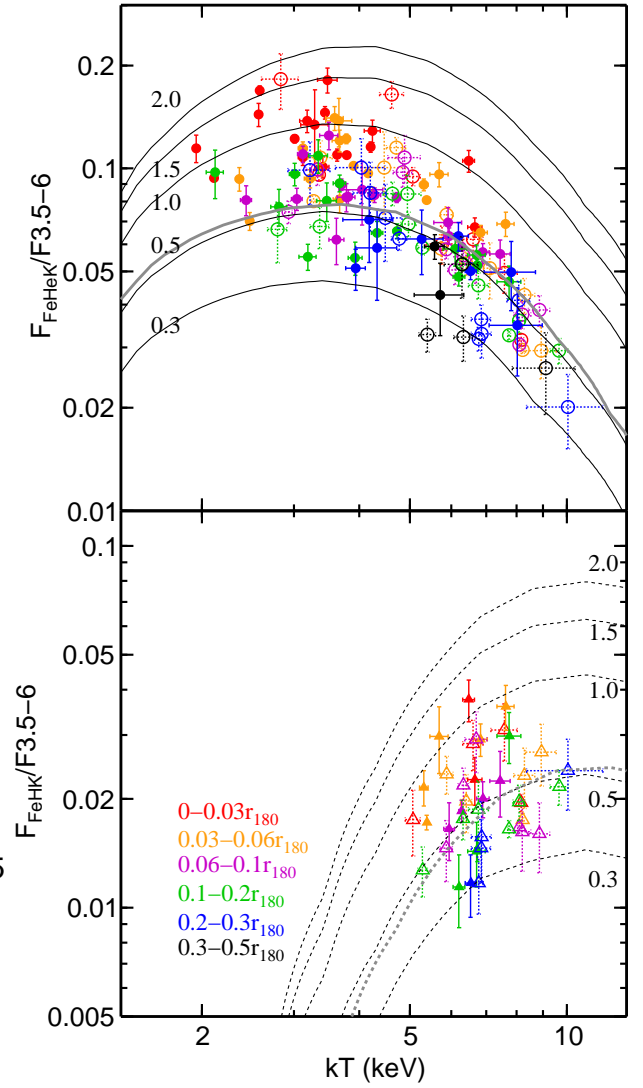


Fig. 4. $F_{\text{FeHeK}}/F_{3.5-6}$ (upper panel; circles) and $F_{\text{FeHK}}/F_{3.5-6}$ (lower panel; triangles) at $0\text{--}0.03r_{180}$ (red), $0.03\text{--}0.06r_{180}$ (orange), $0.06\text{--}0.1r_{180}$ (magenta), $0.1\text{--}0.2r_{180}$ (green), $0.2\text{--}0.3r_{180}$ (blue), and $0.3\text{--}0.5r_{180}$ (black), plotted against the ICM temperature. Closed and open symbols indicate cD clusters and non-cD clusters, respectively. Black solid and dotted lines correspond to the theoretical ratios from the APEC model of $F_{\text{FeHeK}}/F_{3.5-6}$ and $F_{\text{FeHK}}/F_{3.5-6}$, respectively, assuming Fe abundance = 0.3, 0.5, 1.0, 1.5, and 2.0 solar. Here, abundance ratios of elements are assumed to have the solar ratios by Lodders (2003). Those of the MEKAL model assuming Fe abundance = 0.5 solar are plotted as gray lines.

higher than those at $0.06\text{--}0.1r_{180}$ by a factor of 1.5–2. The other non-cD clusters have similar Fe abundances within $0.03r_{180}$ and $0.06\text{--}0.1r_{180}$.

4.4. Temperature dependence of the Fe abundance

In Figure 7 the derived Fe abundances are plotted against the ICM temperature. There is no significant dependence on the plasma temperature, or between the cD and non-cD clusters. The scatter in the Fe abundance tends to be larger

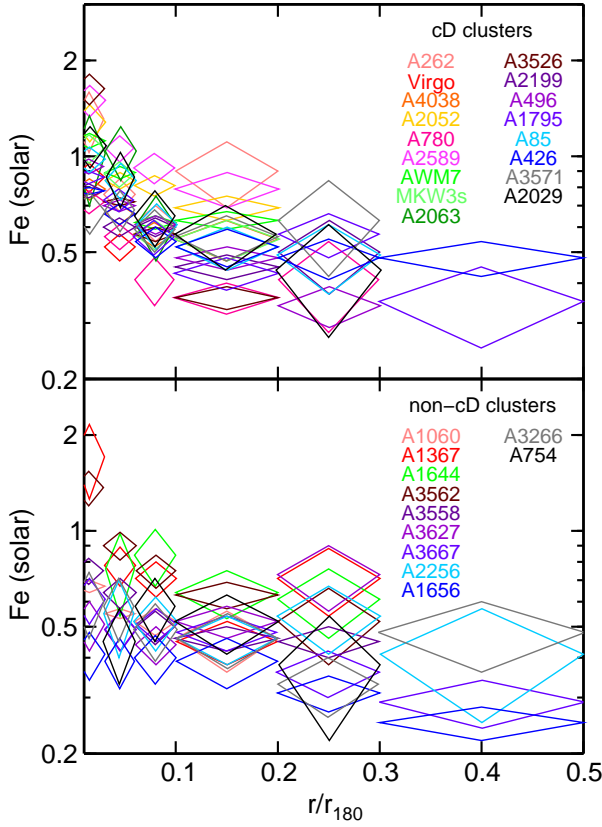


Fig. 5. Radial profiles of the Fe abundances of cD clusters (upper panel) and non-cD clusters (lower panel).

Table 3. Averages of the relative differences in the derived Fe abundances $[(Fe_2 - Fe_1)/Fe_1]$ and their root-mean-square scatters. Cool (hot) samples have local ICM temperatures below (above) 5 keV.

Fe_1	Fe_2	sample	average	scatter
FeHeK, 1T	FeHeK, multi-T	cool	0.01	0.06
FeHeK, 1T	FeHeK, multi-T	hot	0.02	0.10
FeHK, 1T	FeHK, multi-T	hot	-0.04	0.07

in lower temperature clusters. When the ICM temperature is higher than 5 keV, the scatter in the absolute values of the Fe abundances at $0.06-0.3r_{180}$ is small.

4.5. Systematic uncertainties in Fe abundance

In determining the abundance, we must examine uncertainties such as the dependence on the temperature structure and plasma codes.

When the ICM temperature derived from the 1T model was higher than 5 keV, the observed $F_{FeHK}/F_{3.5-6}$ was converted to the Fe abundance as described in Section 4.2. The derived Fe abundances agree well, within statistical errors, with those derived from $F_{FeHeK}/F_{3.5-6}$ (upper panel in Figure 8, Table 2). On average, the difference between the Fe abundances derived from the two lines is only a few %. At the center of the cool core, where the temperature and abundance gradients of the ICM are steep, the Fe abundances derived from the He-like line can be expected to

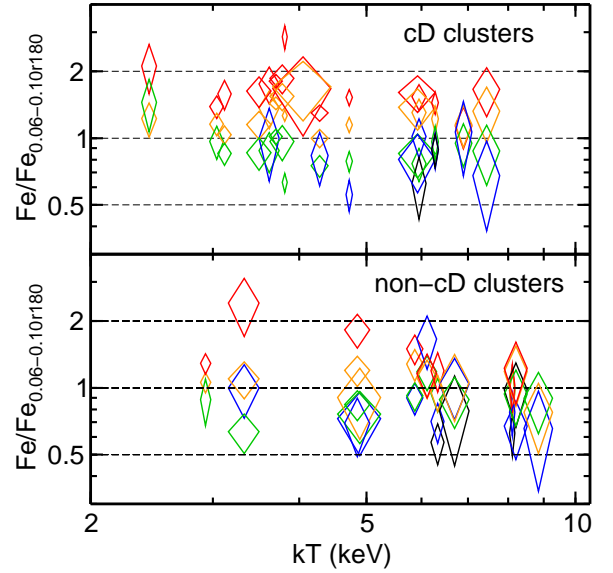


Fig. 6. Ratios of Fe abundances derived from $F_{FeHeK}/F_{3.5-6}$ at $0-0.03r_{180}$ (red), $0.03-0.06r_{180}$ (orange), $0.1-0.2r_{180}$ (green), $0.2-0.3r_{180}$ (blue), and $0.3-0.5r_{180}$ (black) to those at $0.06-0.1r_{180}$, plotted against the ICM temperature at $0.06-0.1r_{180}$. Upper and lower panels correspond to the cD and non-cD clusters, respectively.

be higher than those from the H-like line. However, outside the cool core, where the temperature and abundance gradients weaken, it is reasonable that He-like and H-like lines yield the same Fe abundances. Because the temperature dependence of the He-like and H-like Fe lines are completely different, the consistency of the Fe abundances outside the cool cores indicates a small systematic uncertainty owing to the uncertainties in the ICM temperature.

To examine the systematic effect of the assumptions about the temperature structure, i.e., the 1T model or the multi-T model, we derived the Fe abundance from the observed $F_{FeHeK}/F_{3.5-6}$ and $F_{FeHK}/F_{3.5-6}$ assuming the best-fit multi-T model. For both He-like and H-like lines, the multi-T model yields mostly the same Fe abundances as the 1T model, as summarized in Figure 9 and Table 2. In Figure 9, the error bars arise from a systematic uncertainty of 10% in the ICM temperature, because in most cases these errors are much larger than those from the uncertainty in the multi-T model. Statistical errors in the Fe line strengths are not considered here, because we use the same line strength. As summarized in Table 3, the differences in the Fe abundances from $F_{FeHeK}/F_{3.5-6}$ are smaller than several percent particularly below 5 keV owing to the weaker temperature dependence. Above 5 keV, the systematic differences are still smaller than $\sim 10\%$. The differences in the Fe abundances from $F_{FeHK}/F_{3.5-6}$ are also about several percent owing to the weaker temperature dependence.

Figure 8 also compares the Fe abundances from the two lines, assuming the best-fit multi-temperature model. Here, statistical errors in the line strengths and a 10% systematic uncertainty in the temperature are considered. In most clusters, the two lines yield the same Fe abundances, reflecting that the 1T and multi-T models yielded the same Fe abundances.

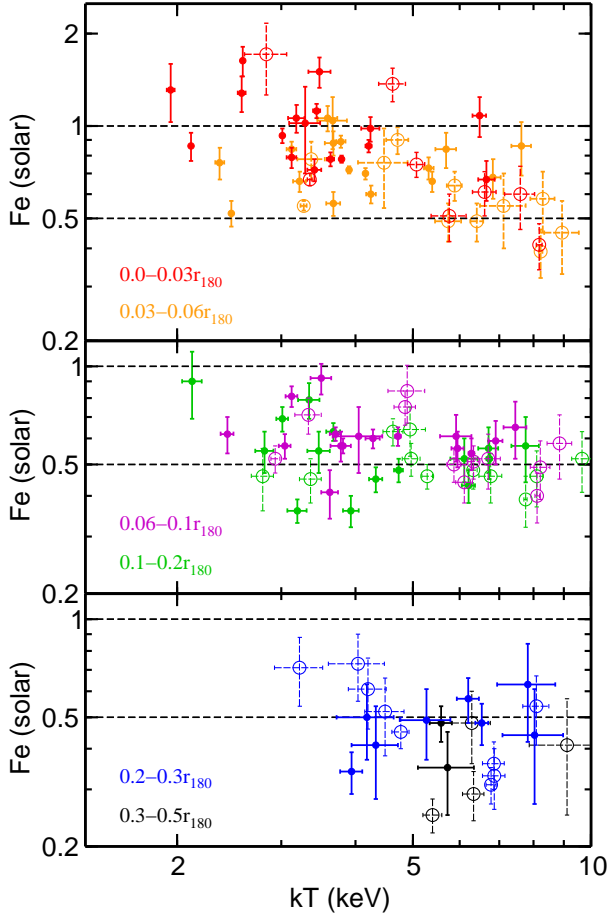


Fig. 7. Fe abundances derived from $F_{\text{FeHeK}}/F_{3.5-6}$ using the 1T APEC model, plotted against the local ICM temperature. The indications of symbols and colors are the same as in Figure 4.

Higher-temperature components may exist in the ICM. Therefore, we left the highest temperature of the multi-T model unconstrained and fitted the spectra from the PN and MOS. For the ICM temperatures from the 1T model below 5 keV we obtained almost the same Fe abundances within several percent. When the ICM temperature is above 5 keV, the Fe abundances using the best-fit multi-T model from the PN spectra were unchanged. However, using the MOS multi-T model, the Fe abundances from the He-like line increased by a several tens of percent, whereas those from the H-like line remained the same within 10%. This discrepancy arises from a systematic uncertainty of several percent in the response matrices of the PN and MOS. Considering the weak temperature dependence of the $F_{\text{FeHeK}}/F_{3.5-6}$ at higher temperatures, the Fe abundances from the H-like line are more reliable outside the cool core regions.

Rasia et al. (2008) studied bias or systematic effects in the X-ray spectra using the spectra simulated by the X-ray Map Simulator and found that the Fe abundance is recovered with high accuracy for hot ($T > 3$ keV) and cold ($T < 2$ keV) systems. At intermediate temperatures ($2 \text{ keV} < T < 3 \text{ keV}$), they found systematic overestimates. The problem occurs because of a transition between the relative importance of the Fe-L and Fe-K lines. Because we here derived

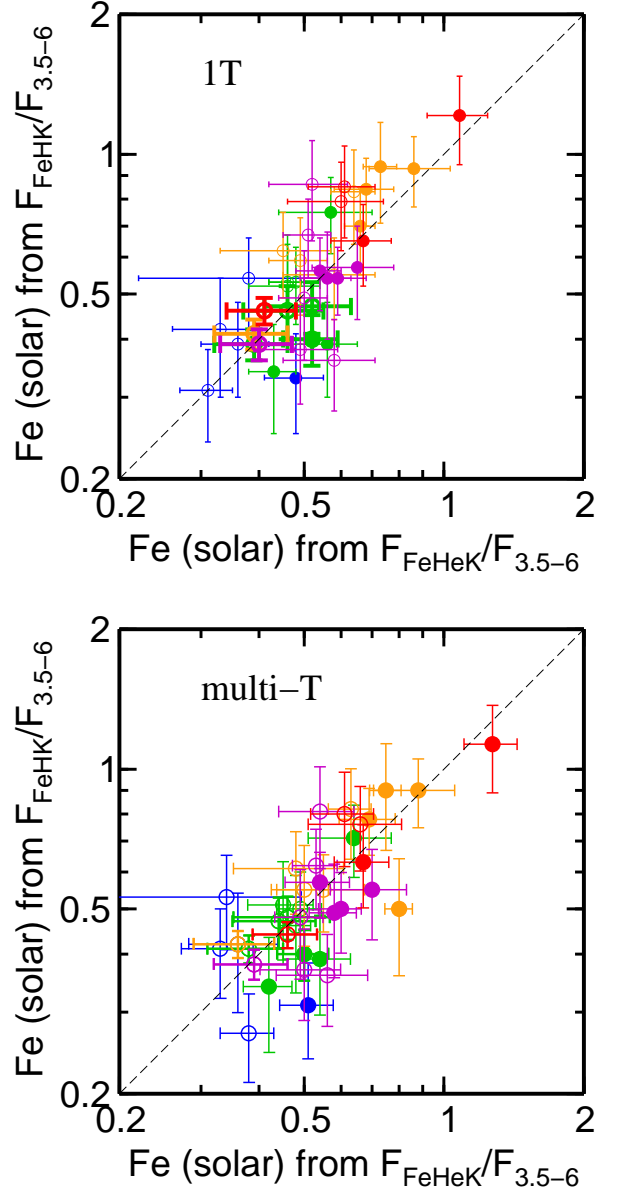


Fig. 8. Fe abundances derived from $F_{\text{FeHeK}}/F_{3.5-6}$ versus those from $F_{\text{FeHeK}}/F_{3.5-6}$, using the 1T model (upper panel) and the best-fit multi-T model (lower panel). A systematic uncertainty of 10% in the temperature is considered. The indications of colors are the same as in Figure 4. Closed and open circles correspond to cD and non-cD clusters, respectively.

the Fe abundances from the Fe-K lines, the observed values do not include those of the coolest components (below ~ 1.7 keV). The fraction of the emission measure for temperature components below this temperature is smaller than several percent except in the innermost region of the coolest cool cores of the Virgo cluster and A 262, where the fractions are 30%.

To examine the systematic effect of the plasma code on abundance determination, we plotted the temperature dependence of the ratio of line strength to $F_{3.5-6}$ in Figure 4 using the MEKAL model (Mewe et al. 1995, 1996; Kaastra

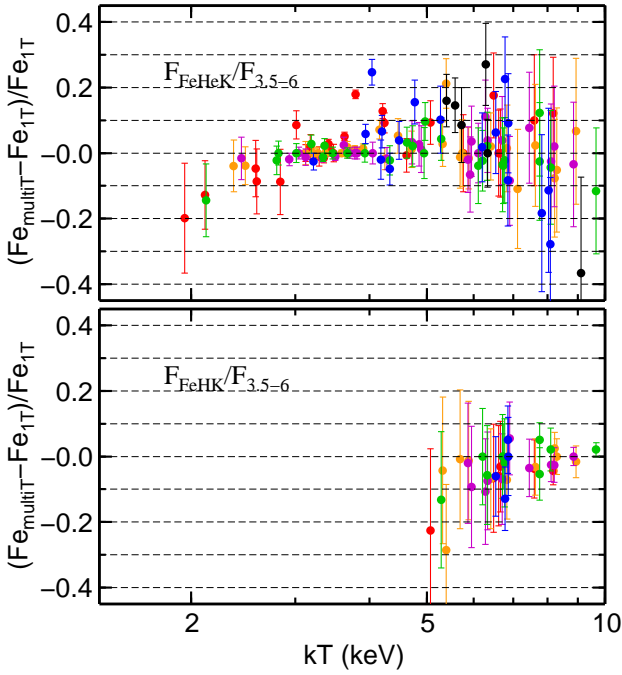


Fig. 9. Differences between the derived Fe abundances using the best-fit multi-T model and those using the 1T model, plotted against the ICM temperature. Error bars are the result of uncertainties in the ICM temperature derived from the 1T model, including systematic uncertainties of 10%. Upper and lower panels correspond to Fe abundances derived from $F_{\text{FeHeK}}/F_{3.5-6}$ and $F_{\text{FeHK}}/F_{3.5-6}$, respectively. The indications of the colors are the same as in Figure 4.

1992; Liedahl et al. 1995). The difference between the MEKAL and APEC models is less than 10%.

Non-solar abundance ratios of He, C, N, and O to Fe cause a bias in the derived Fe abundance, since these elements change the continuum level. The difference in the He abundance between the solar abundance tables by Lodders (2003) and Anders & Grevesse (1989) yields a bias of several percent. The bias resulting from a possible high He-abundance in the ICM is discussed in detail in Ettori & Fabian (2006) and Böhringer & Werner (2010).

In summary, in most cases, the systematic uncertainty in the derived Fe abundances caused by the uncertainties in the temperature structures and atomic data is about 10%.

4.6. Weighted average of Fe abundance profiles

We calculated the weighted average of the Fe abundances derived from $F_{\text{FeHeK}}/F_{3.5-6}$ and $F_{\text{FeHK}}/F_{3.5-6}$, using the 1T APEC model within the same radial region in the units of r_{180} . We divided the clusters except for A426 (the Perseus cluster) and A1656 (the Coma cluster) according to whether they are cD or non-cD clusters.

The results are summarized in Table 4 and Figure 10. The radial profile of the average Fe abundance of the cD clusters becomes flatter from 0.1 to 0.3 r_{180} at 0.4–0.5 solar. The Perseus cluster has a 10% smaller radial profile than the other cD clusters within 0.3 r_{180} , and a flatter Fe abundance profile up to 0.5 r_{180} . In contrast, the non-cD

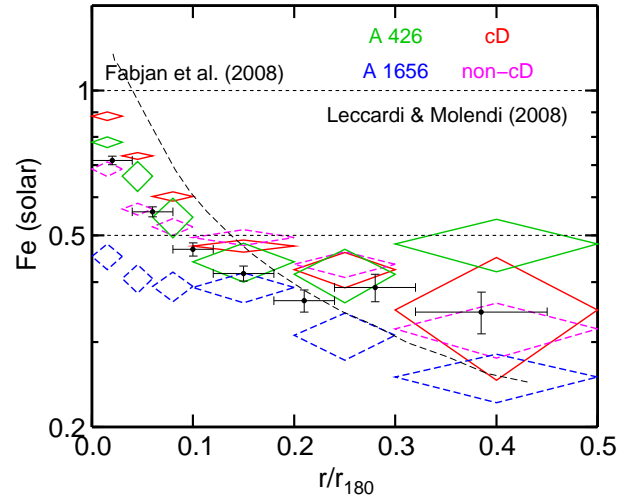


Fig. 10. Fe abundance profiles of A426 (green), A1656 (blue), and the averages of those of cD clusters (red solid diamonds) and non-cD clusters (magenta dashed diamonds) in our sample, compared with the average profile of $z=0.1\sim0.3$ clusters (black closed circles) from Leccardi & Molendi (2008). Black dashed line corresponds to the Fe abundance derived from the numerical simulations without AGN feedback by Fabjan et al. (2008).

clusters have systematically lower Fe abundances within 0.1 r_{180} , and the values similar to those of cD clusters beyond this radius. The Coma cluster also has a flatter radial profile within 0.2 r_{180} , but at a lower value of ~ 0.4 solar, and beyond this radius, the Fe abundance gradually decreases to ~ 0.3 solar.

Table 4. Weighted average of Fe abundances derived from $F_{\text{FeHeK}}/F_{3.5-6}$ and $F_{\text{FeHK}}/F_{3.5-6}$, in the units of the solar abundance.

radius ^a	cDs ^b	A 426	non-cDs ^c	A 1656
0.00-0.03	0.88 ± 0.02	0.78 ± 0.01	0.69 ± 0.02	0.45 ± 0.03
0.03-0.06	0.73 ± 0.01	0.66 ± 0.05	0.57 ± 0.02	0.41 ± 0.03
0.06-0.10	0.60 ± 0.01	0.55 ± 0.05	0.52 ± 0.02	0.39 ± 0.03
0.10-0.20	0.48 ± 0.01	0.44 ± 0.04	0.50 ± 0.02	0.39 ± 0.03
0.20-0.30	0.42 ± 0.04	0.41 ± 0.05	0.44 ± 0.03	0.31 ± 0.03
0.30-0.50	0.35 ± 0.10	0.48 ± 0.06	0.32 ± 0.04	0.25 ± 0.03

^a: in unit of r_{180} .

^b: the cD clusters except A 426

^c: the non-cD clusters except A 1656

4.7. Comparison with previous papers and redshift evolution

In Figure 10 we compare our results with those obtained by Leccardi & Molendi (2008). Here, the Fe abundances were scaled using Lodders (2003), considering the difference in the solar values of He and Fe. Leccardi and Molendi (2008) analyzed ~ 50 hot ($kT > 3.3$ keV) intermediate-redshift ($z = 0.1 \sim 0.3$) clusters of galaxies observed with XMM-Newton. Although we use samples different from those employed by Leccardi & Molendi (2008), our mean profiles of

the cD clusters and those of Leccardi & Molendi (2008) have remarkably similar slopes, but the absolute values differ by 10–20%.

Maughan et al. (2008) analyzed redshift evolution up to $z \sim 1$ of the Fe abundance in the ICM using Chandra observations. The mean value of Maughan et al. (2008) at $0.15-1r_{500}$ of $z < 0.5$ clusters is ~ 0.5 solar using the solar abundance by Lodders (2003), and is consistent with the average of the cD clusters.

These agreements indicate that the evolution of the Fe abundance with redshift from $z = 0$ to $z = 0.5$ is consistent with no evolution within our systematic uncertainties. The expected evolution according to Ettori (2005), which is about 30% from $z \sim 0.5$ to $z \sim 0$, tends to be larger than our observations.

5. Discussion

5.1. Flatter radial Fe abundance profile beyond $0.1r_{180}$

Beyond $0.1r_{180}$, well outside the cool cores, both the cD and non-cD clusters have similar Fe abundance profiles with a relatively small scatter. Within $0.1-0.3r_{180}$, the Fe abundances of the sample clusters are $0.4-0.5$ solar. There is no dependence on the ICM temperature, i.e., system richness. In other words, outside the central regions of clusters, the Fe abundance in the ICM may be universal in clusters of galaxies, and clusters of galaxies may have universal metal-enrichment histories. Beyond $0.3r_{180}$, the Fe abundances become $0.2-0.5$ solar. These profiles smoothly connect with the Suzaku observations of the Fe distributions in the ICM beyond $0.5r_{180}$ (Fujita et al. 2008; Tawa 2008).

The distribution of Fe abundance in the ICM has been modeled via hydrodynamic simulations (Fabjan et al. 2008, Kapferer et al. 2007). Figure 10 also compares our mean Fe abundance profiles with that derived by Fabjan et al. (2008). Beyond $0.1r_{180}$, the profile simulated by Fabjan et al. (2008) continues to decrease outward, whereas the observed profile becomes flatter.

The iron-mass-to-light ratio (IMLR), i.e., the ratio of Fe mass in the ICM to total stellar luminosity, is important for studying the origin of Fe, because Fe is synthesized in stars. The integrated values of the IMLR profiles of the $kT \sim 3$ keV clusters, Abell 262, and AWM7, observed with Suzaku (Sato et al. 2008, 2009), increase outward from $0.1r_{180}$ to $0.3-0.4r_{180}$. This result indicates that Fe in the ICM extends farther than stars in the outer regions at least in these two clusters.

A simple explanation is that a significant fraction of Fe is synthesized in an early phase of cluster evolution. If metal enrichment occurs after the formation of the clusters, the metal distribution is expected to follow the stellar distribution, whereas if it occurs before cluster formation, we expect a flatter distribution. For example, simulations by Kapferer et al. (2007) yielded a flatter Fe profile from SN II. That the measurements of the Fe abundance excluding the central region by Maughan et al. (2008) are consistent with no evolution at least up to $z=0.7$ also supports the early synthesis of Fe. Feedback by active galactic nuclei (AGN) may also change the abundance profile. With AGN feedback, a flatter radial profile beyond $0.1r_{180}$ is also obtained in the simulation by Fabjan et al. (2010).

A426 (the Perseus cluster) shows a completely flat Fe profile from $0.1r_{180}$ to $0.5r_{180}$: at $0.3-0.5r_{180}$, the Fe abun-

dance is higher than in the other clusters. Within the annular region of $0.3-0.5r_{180}$, the observed fields of view do not cover the entire annular region (Figure 1) and lack the north and south regions. Several clusters, including A426, form the Perseus supercluster, which is elongated in an east-west direction (Gregory et al. 1981). The observed very flat Fe abundance may reflect the history of cluster formation from filaments of the large-scale structure of the Universe.

5.2. Fe profiles within the cool core regions

Fe in the gas in the cool core of clusters is a mixture of that present in the ICM and later supplies from their cD galaxies. The latter contains Fe synthesized by SN Ia and originating from stars through stellar mass loss, because Fe is synthesized by both SN Ia and SN II. According to abundance patterns from XMM-Newton observations of the cool cores (Matsushita et al. 2003, 2007; Werner et al. 2006; de Plaa et al. 2006; Simionescu et al. 2008, 2009) and Suzaku observations of the cD galaxies of AWM7 and A262 (Sato et al. 2008, 2009), the number ratio of SNe II to SNe Ia is estimated to be $3-4$, and the Fe in the cluster core was synthesized mostly by SN Ia.

Within cool core regions, clusters have negative abundance gradients (e.g. Fukazawa et al. 2000, de Grandi et al. 2004). Rossetti & Molendi (2010) and Leccardi, Rossetti, & Molendi (2010) also found central metal abundance excess in low-entropy core systems. Within these regions, observations indicate that metals ejected from cD galaxies have a more extensive distribution compared with stars. Analyzing eight cool-core clusters observed with XMM, David & Nulsen (2008) found that Fe in the ICM is more extended than the stellar mass, and excess Fe within the central 100 kpc could have been produced by type Ia supernova in cD galaxies over the past 3–7 Gyr. The IMLR values in AWM7 and A262 observed with Suzaku have much steeper positive gradients within the cool cores than those beyond $0.1r_{180}$ (Sato et al. 2008; 2009).

Processes such as jets from a central AGN as described below, or the “sloshing” of cD galaxies in the cluster’s gravitational potential (e.g. Markevitch et al. 2001), may eject metals from cD galaxies. On the basis of 2D temperature and metallicity maps of M 87 (Simionescu et al. 2008) and Hydra A (Simionescu et al. 2009), uplift of Fe by the AGN was discussed in detail. David & Nulsen (2008) found that both turbulent diffusion of entropy and dissipation are important heating mechanisms in cluster cores. Rebusco et al. (2006) compared the observed Fe abundance profiles with the predictions of a model involving metal ejection from the brightest galaxy and the subsequent diffusion of metals by stochastic gas motions. Roediger et al. (2007) studied the effect of bubble-induced motions on metallicity profiles through 3D hydro simulations. The new simulation by Fabjan et al. (2010) showed a less steep central Fe peak including feedback from AGN in cD galaxies. The observed small scatter in the Fe abundance slope within $0.1r_{180}$ in the cD clusters suggests a common process of metal supply and ejection in the cD galaxies. The next Japanese X-ray satellite, ASTRO-H, will directly reveal line broadening caused by turbulence in the cores of clusters.

Peng & Nagai (2009) pointed out that the He/H abundance ratio could be four times the solar abundance at the center of massive clusters. Such a high He abundance causes an underestimation of the Fe abundance by a factor of two

(Ettori & Fabian 2006). However, in actual clusters, metals at the center of the cluster come from mass loss by central galaxies, and in addition, more extensively distributed compared with stars. Therefore, the centers of clusters should not be static, as assumed in the calculations of Peng & Nagai (2009).

5.3. Mixing of the ICM in non-cD clusters

Most of clusters without cool cores tend to show no central abundance excess as found in Fukazawa et al. (2000); de Grandi et al. (2004). Leccardi, Rossatti & Molendi (2010) found that some medium- and high-entropy core systems have central abundance excess, most of which are undergoing a phase of rapid dynamical changes, and suggested that these clusters originate from low-entropy core systems.

Our results are consistent with the discussion in Leccardi, Rossatti & Molendi (2010). The non-cD clusters in this paper include merging clusters in various stages, from heavily distorted morphologies to relatively relaxed ones without cool cores. During cluster merging, mixing of the ICM could destroy the central Fe peak. Clusters with the highest central Fe abundances have highly disturbed morphologies. In the first stage of merging, the Fe peak and the cool core may remain. Then, mixing of the ICM destroys the Fe peak, and the Fe abundance becomes flat at the same level as in cD clusters at $0.1\text{--}0.5r_{180}$.

6. Summary and conclusion

We derived radial profiles of the Fe abundance of the ICM in nearby ($z < 0.08$) clusters observed with XMM-Newton. The Fe abundances of the ICM were derived from the ratio of the flux of the $K\alpha$ lines of He-like or H-like Fe to those of the continuum at 3.5–6.0 keV, because the systematic uncertainty in the continuum flux in this energy band owing to the background is smaller. The temperature dependence of these ratios constrains the Fe abundances of multi-temperature plasmas.

In cluster core regions ($< 0.1r_{180}$), the observed Fe abundances of cD clusters show similar radial profiles. The less-peaked abundance profile compared with the light in the central region indicates the ejection of metals from cD galaxies.

In the outer regions, $0.1\text{--}0.2r_{180}$, Fe abundances of 0.4–0.5 solar appear to be universal with no temperature dependence. The observed flatter Fe abundance profiles of the cD clusters beyond $0.1r_{180}$ indicate early metal enrichment.

Chandra and XMM cannot reach beyond $0.5r_{180}$ owing to a high, unstable particle background. Information is available for only about 10% of the cluster volume, and the majority has not yet been revealed. The total amount of Fe synthesized in galaxies can be derived only by the precise abundance measurements beyond $0.5r_{180}$. Because of its low background, Suzaku is the only satellite available for the next several years to study clusters of galaxies up to the virial radius. With Suzaku, Fe abundances will be determined out to a radius of $0.7\sim 0.8r_{180}$.

References

Anders, E., & Grevesse, N. 1989, *Geochim. Cosmochim. Acta*, 53, 197
 Arnaud, M., Rothenflug, R., Boulade, O., Vigroux, L., & Vangioni-Flam, E. 1992, *A&A*, 254, 49

Baldi, A., Ettori, S., Mazzotta, P., Tozzi, P., & Borgani, S. 2007, *ApJ*, 666, 835
 Böhringer, H., Matsushita, K., Churazov, E. et al. 2002, *A&A*, 382, 804
 Böhringer, H., & Werner, N. 2010, *A&A Rev.*, 18, 127
 David, L. P., & Nulsen, P. E. J. 2008, *ApJ*, 689, 837
 De Grandi, S., Ettori, S., Longhetti, M., & Molendi, S. 2004, *A&A*, 419, 7
 de Plaa, J., et al. 2006, *A&A*, 452, 397
 Dickey, J. M., & Lockman, F. J. 1990, *ARA&A*, 28, 215
 Ebeling, H., Voges, W., Böhringer, H., Edge, A. C., Huchra, J. P., & Briel, U. G. 1996, *MNRAS*, 281, 799
 Ettori, S. 2005, *MNRAS*, 362, 110
 Ettori, S., & Fabian, A. C. 2006, *MNRAS*, 369, L42
 Ezawa, H., Fukazawa, Y., Makishima, K., Ohashi, T., Takahara, F., Xu, H., & Yamasaki, N. Y. 1997, *ApJ*, 490, L33
 Ezawa, H., et al. 2001, *PASJ*, 53, 595
 Fabjan, D., Tornatore, L., Borgani, S., Saro, A., & Dolag, K. 2008, *MNRAS*, 386, 1265
 Fabjan, D., Borgani, S., Tornatore, L., Saro, A., Murante, G., & Dolag, K. 2010, *MNRAS*, 401, 1670
 Finoguenov, A., David, L. P., & Ponman, T. J. 2000, *ApJ*, 544, 188
 Finoguenov, A., Arnaud, M., & David, L. P. 2001, *ApJ*, 555, 191
 Fujita, Y., Tawa, N., Hayashida, K., Takizawa, M., Matsumoto, H., Okabe, N., & Reiprich, T. H. 2008, *PASJ*, 60, 343
 Fukazawa, Y., Makishima, K., Tamura, T., Ezawa, H., Xu, H., Ikebe, Y., Kikuchi, K., & Ohashi, T. 1998, *PASJ*, 50, 187
 Fukazawa, Y., Makishima, K., Tamura, T., Nakazawa, K., Ezawa, H., Ikebe, Y., Kikuchi, K., & Ohashi, T. 2000, *MNRAS*, 313, 21
 Gregory, S. A., Thompson, L. A., & Tifft, W. G. 1981, *ApJ*, 243, 411
 Kaastra J.S. 1992, *An X-Ray Spectral Code for Optically Thin Plasmas* (Internal SRON-Leiden Report, updated version 2.0)
 Katayama, H., Takahashi, I., Ikebe, Y., Matsushita, K., & Freyberg, M. 2004, *A&A*, 414, 767
 Kapferer, W., et al. 2007, *A&A*, 466, 813
 Leccardi, A., & Molendi, S. 2008, *A&A*, 487, 461
 Leccardi, A., Rossetti, M., & Molendi, S. 2010, *A&A*, 510, A82
 Liedahl D. A., Osterheld A.L., & Goldstein W.H. 1995, *ApJ*, 438, L115
 Lodders, K. 2003, *ApJ*, 591, 1220
 Lumb, D. H., Warwick, R. S., Page, M., & De Luca, A. 2002, *A&A*, 389, 93
 Matsushita, K., Finoguenov, A., Böhringer, H. 2003, *A&A*, 401, 443
 Matsushita, K., Böhringer, H., Takahashi, I., & Ikebe, Y. 2007, *A&A*, 462, 953
 Mewe R., Gronenschild E.H.B.M., & van den Oord G.H.J. 1985, *A&AS*, 62, 197
 Mewe R., Lemen J.R., & van den Oord, G.H.J. 1986, *A&AS*, 65, 511
 Makishima, K., Ezawa, H., Fukuzawa, Y., Honda, H., Ikebe, Y., Kamae, T., Kikuchi, K., Matsushita, K., Nakazawa, K., Ohashi, T., Takahashi, T., Tamura, T. & Xu, H. 2001, *PASJ*, 53, 401
 Markevitch, M., Forman, W. R., Sarazin, C. L., & Vikhlinin, A. 1998, *ApJ*, 503, 77
 Markevitch, M., Vikhlinin, A., & Mazzotta, P. 2001, *ApJ*, 562, L153
 Maughan, B. J., Jones, C., Forman, W., & Van Speybroeck, L. 2008, *ApJS*, 174, 117
 Peng, F., & Nagai, D. 2009, *ApJ*, 693, 839
 Rasia, E., Mazzotta, P., Bourdin, H., Borgani, S., Tornatore, L., Ettori, S., Dolag, K., & Moscardini, L. 2008, *ApJ*, 674, 728
 Rebusco, P., Churazov, E., Böhringer, H., & Forman, W. 2006, *MNRAS*, 372, 1840
 Reese, E. D., Kawahara, H., Kitayama, T., Ota, N., Sasaki, S., & Suto, Y. 2010, *ApJ*, 721, 653
 Renzini, A., Ciotti, L., D’Ercole, A., & Pellegrini, S. 1993, *ApJ*, 419, 52
 Roediger, E., Brüggén, M., Rebusco, P., Böhringer, H., & Churazov, E. 2007, *MNRAS*, 375, 15
 Rossetti, M., & Molendi, S. 2010, *A&A*, 510, A83
 Sato, K., Matsushita, K., Ishisaki, Y., Yamasaki, N. Y., Ishida, M., Sasaki, S., & Ohashi, T. 2008, *PASJ*, 60, 333
 Sato, K., Matsushita, K., & Gastaldello, F. 2009, *PASJ*, 61, 365
 Simionescu, A., Werner, N., Finoguenov, A., Böhringer, H., & Brüggén, M. 2008, *A&A*, 482, 97
 Simionescu, A., Werner, N., Böhringer, H., Kaastra, J. S., Finoguenov, A., Brüggén, M., & Nulsen, P. E. J. 2009, *A&A*, 493, 409
 Smith, R.K., Brickhouse, N.S., Liedahl, D.A., & Raymond, J.S., 2001, *ApJ*, 556, 91
 Snowden S. L., Mushotzky R. F., Kuntz K. D., Davis D. S., 2008, *A&A*, 478, 615

- Tanaka, Y., Inoue, H., & Holt, S. S. 1994, PASJ, 46, L37
- Tamura, T., Kaastra, J. S., den Herder, J. W. A., Bleeker, J. A. M., & Peterson, J. R. 2004, A&A, 420, 135
- Tawa, N., 2008, PhD thesis, University of Osaka
- Vikhlinin, A., Markevitch, M., Murray, S. S., Jones, C., Forman, W., & Van Speybroeck, L. 2005, ApJ, 628, 655
- Werner, N., de Plaa, J., Kaastra, J. S., Vink, J., Bleeker, J. A. M., Tamura, T., Peterson, J. R., & Verbunt, F. 2006, A&A, 449, 475
- Yoshino, T., et al. 2009, PASJ, 61, 805 W
- Zhang, Y.-Y., Reiprich, T. H., Finoguenov, A., Hudson, D. S., & Sarazin, C. L. 2009, ApJ, 699, 1178

Table 1. Cluster samples in the XMM-Newton archival data

cluster	z	$\langle T \rangle^a$ (keV)	N_H^b (10^{20} cm^{-2})	type ^c	obsid (exposures of PN, MOS1 and MOS2) ^d (ks, ks, ks)
A262	0.016	2.5	5.4	cD	0109980101 (19.0 23.6 23.9) 0504780201 (24.9 31.6 33.1)
Virgo	0.004	2.8	2.6	cD	0114120101 (30.0 37.7 38.5) 0200920101 (69.6 76.9 78.5)
					0106060101 (5.0 9.2 9.2) 0106060201 (1.6 5.5 5.0) 0106060301 (5.4 7.1 7.9)
					0141570101 (17.4 23.2 24.7) 0112550701 (1.0 0.2) 0112552101 (7.6 13.4 13.5)
					0106060401 (7.3 10.7 11.1) 0145800101 (5.9 37.8 0.2 0.2) 0106060501 (10.9 15.3 15.4)
					0200650101 (42.7 53.2 53.5) 0112840101 (14.6 18.1 17.6) 0106060601 (8.6 10.5 10.7)
					0112550801 (2.9 13.2 12.1) 0106060701 (1.2 12.4 5.9) 0108860101 (16.7 20.6 19.2)
					0106061401 (4.9 8.0 8.3)
A4038	0.029	3.0	1.5	cD	0204460101 (27.8 29.3 28.9)
A1060	0.012	3.0	4.9	non-cD	0206230101 (28.5 37.9 38.9)
A2052	0.035	3.1	3.0	cD	0109920101 (26.4 28.9 29.0)
A1367	0.021	3.3	2.4	non-cD	0061740101 (23.7 31.8 31.4) 0005210101 (20.8 27.8 28.8)
A780	0.057	3.5	4.7	cD	0109980301 (14.0 19.1 22.2)
A2589	0.042	3.6	3.9	cD	0204180101 (21.8 26.3 27.5)
AWM7	0.017	3.6	9.8	cD	0135950301 (27.5 30.7 30.9)
MKW3s	0.045	3.7	3.0	cD	0109930101 (0.0 37.7 38.0)
A2063	0.036	3.9	3.0	cD	0200120401 (5.0 8.2 5.0)
A3526	0.010	4.0	8.2	cD	0046340101 (35.2 44.9 43.5) 0406200101 (90.5 111.7 111.7) 0504360101 (26.4 28.2 30.9)
					0504360201 (32.9 34.0 34.6)
A2199	0.030	4.2	0.9	cD	0008030601 (0.5 6.9 4.7) 0008030301 (2.9 4.7 4.7) 0008030201 (13.3 14.5 14.6)
A496	0.033	4.4	4.6	cD	0135120201 (11.8 16.2 15.9) 0506260301 (44.5 57.0 59.5) 0506260401 (44.8 55.8 58.6)
A1644	0.048	4.6	4.8	non-cD	0010420201 (12.7 14.1 14.1)
A3562	0.050	4.8	4.0	non-cD	0105261301 (37.7 39.0 39.5) 0105261501 (4.8 22.4 22.4) 0105261801 (4.7 10.9 10.4)
					0105261701 (0.0 20.6 20.4) 0105261601 (16.3 18.3 19.5) 0105261401 (9.0 12.8 12.4)
A3558	0.048	5.4	4.2	non-cD	0107260101 (38.2 43.1 42.5)
A3627	0.016	5.5	20.8	non-cD	0204250101 (2.4 6.2 5.8) 0208010101 (9.1 12.6 13.0) 0208010201 (10.9 13.6 14.3)
A1795	0.062	5.8	1.2	cD	0097820101 (25.1 38.3 37.9) 0109070201 (53.0 54.5 54.6) 0205190101 (26.9 29.5 28.8)
					0205190201 (20.8 22.6 23.2)
A85	0.052	5.8	3.1	cD	0065140101 (9.8 12.4 12.2) 0065140201 (9.2 12.1 12.4)
A3667	0.053	6.0	4.6	non-cD	0105260101 (0.8 7.3 6.8) 0206850101 (52.3 59.2 60.0) 0105260601 (17.7 23.1 23.3)
					0105260301 (12.8 17.0 16.2) 0105260401 (11.5 16.3 16.5) 0105260501 (11.2 12.6 12.6)
					0105260201 (15.1 19.0 18.4)
A426 (Perseus)	0.018	6.1	14.6	cD	0085110101 (47.5 48.8 50.7) 0204720101 (11.9 15.1 15.2) 0085590201 (38.4 41.7 40.0)
					0305720101 (10.0 13.0 12.6) 0305720301 (15.9 19.9 21.2) 0151560101 (18.0 24.9 25.1)
					0204720201 (20.7 24.5 24.5) 0405410201 (9.4 17.3 25.5) 0405410101 (12.2 18.2 16.1)
A2256	0.058	6.3	4.1	non-cD	0141380101 (6.4 9.2 8.7) 0141380201 (10.6 13.2 12.4)
					0112951501 (5.9 10.6 10.9) 0112951601 (7.2 12.7 12.7) 0112950601 (8.4 12.3 11.8)
					0112500101 (21.8 25.0 25.2)
A3571	0.040	6.5	4.4	cD	0086950201 (14.3 25.4 25.2)
A2029	0.077	7.4	3.2	cD	0111270201 (9.3 12.1 12.4)
A1656 (Coma)	0.023	7.8	0.9	non-cD	0300530201 (0.4 3.6 3.4) 0153750101 (19.2 21.3 21.8) 0124711401 (14.7 17.4 16.5)
					0300530101 (18.6 20.9 21.0) 0300530301 (26.5 30.5 30.2) 0300530701 (16.4 24.4 24.6)
					0300530401 (13.3 18.8 19.6) 0300530601 (16.7 22.6 22.1) 0300530501 (19.2 24.7 24.6)
					0124710901 (16.7 21.6 22.1) 0124712001 (9.2 15.4 14.6) 0124710501 (10.7 24.4 24.8)
					0124710601 (4.7 9.5 9.0) 0204040101 (69.7 73.0 74.0) 0204040301 (43.7 52.9 53.2)
					0204040201 (54.8 61.8 64.8) 0124710801 (18.4 24.5 24.5) 0124710401 (8.2 5.9 5.6)
					0124712501 (23.8 27.7 27.7) 0124712401 (11.0 17.4 18.1) 0124711101 (13.2 19.3 21.1)
					0124712201 (18.2 26.7 26.2) 0124712101 (20.3 26.0 26.1) 0124710301 (10.6 13.4 14.0)
					0124710101 (23.7 30.6 30.8)
A3266	0.055	8.4	1.5	non-cD	0105262201 (3.4 0.0 3.6) 0105260901 (18.6 24.4 24.3) 0105260801 (16.2 19.6 20.4)
					0105262501 (3.5 7.6 7.7) 0105262001 (2.9 7.6 7.6) 0105260701 (16.1 20.6 20.5)
					0105261101 (8.0 12.7 11.1) 0105262101 (4.4 5.6 7.2)
A754	0.054	8.6	4.7	non-cD	0112950301 (8.0 13.3 13.7) 0112950401 (7.6 14.3 14.3) 0136740201 (2.3 6.0 6.7)
					0136740101 (12.5 14.2 14.2)

^a: Adopted average temperature of ICM used to calculate r_{180} .^b: The Galactic value of the hydrogen column density (Dickey & Lockman 1990)^c: “cD” corresponds to cD clusters, which are relaxed clusters with a cD galaxy at their center. Other clusters are classified as “non-cD.”^d: obsid (a unique XMM-Newton observation identifier) and exposure times of PN, MOS1, and MOS2, respectively, after screening out the background flares.

Table 2. Results of spectral fitting of annular spectra.

cluster	r (r_{180})	kT^a (keV)	Fe (solar) from $F_{\text{FeHeK}}/F_{3.5-6}$ Best-fit ^b $\pm \Delta_{\text{stat}}^c \Delta_{\text{sys}}^d$	Fe (solar) from $F_{\text{FeHK}}/F_{3.5-6}$ Best-fit ^b $\pm \Delta_{\text{stat}}^c \Delta_{\text{sys}}^d$
A262	0.00-0.03	1.95 \pm 0.03	1.31 \pm 0.28-0.26	—
A262	0.03-0.06	2.36 \pm 0.04	0.76 \pm 0.09-0.03	—
A262	0.06-0.10	2.43 \pm 0.06	0.62 \pm 0.08-0.02	—
A262	0.10-0.20	2.12 \pm 0.08	0.90 \pm 0.21-0.13	—
Virgo	0.00-0.03	2.11 \pm 0.00	0.86 \pm 0.09-0.11	—
Virgo	0.03-0.06	2.47 \pm 0.01	0.52 \pm 0.05-0.02	—
A4038	0.00-0.03	3.12 \pm 0.06	0.79 \pm 0.06+0.00	—
A4038	0.03-0.06	3.22 \pm 0.08	0.66 \pm 0.05+0.00	—
A4038	0.06-0.10	3.04 \pm 0.07	0.57 \pm 0.05+0.00	—
A4038	0.10-0.20	2.81 \pm 0.10	0.55 \pm 0.08+0.01	—
A1060	0.00-0.03	3.35 \pm 0.03	0.67 \pm 0.03-0.01	—
A1060	0.03-0.06	3.27 \pm 0.04	0.55 \pm 0.02-0.00	—
A1060	0.06-0.10	2.93 \pm 0.05	0.52 \pm 0.05-0.01	—
A1060	0.10-0.15	2.79 \pm 0.12	0.46 \pm 0.10-0.01	—
A2052	0.00-0.03	2.57 \pm 0.04	1.28 \pm 0.17-0.07	—
A2052	0.03-0.06	3.12 \pm 0.06	0.84 \pm 0.05-0.00	—
A2052	0.06-0.10	3.12 \pm 0.07	0.81 \pm 0.06-0.00	—
A2052	0.10-0.20	3.01 \pm 0.07	0.69 \pm 0.06-0.01	—
A1367	0.00-0.03	2.83 \pm 0.23	1.71 \pm 0.45-0.15	—
A1367	0.03-0.06	3.37 \pm 0.18	0.78 \pm 0.11+0.00	—
A1367	0.06-0.10	3.33 \pm 0.17	0.71 \pm 0.09-0.01	—
A1367	0.10-0.20	3.36 \pm 0.14	0.45 \pm 0.07+0.00	—
A1367	0.20-0.30	3.22 \pm 0.30	0.71 \pm 0.17-0.02	—
A780	0.00-0.03	3.41 \pm 0.09	0.72 \pm 0.06+0.02	—
A780	0.03-0.06	3.67 \pm 0.10	0.56 \pm 0.05+0.01	—
A780	0.06-0.10	3.62 \pm 0.12	0.41 \pm 0.07+0.01	—
A780	0.10-0.20	3.93 \pm 0.12	0.36 \pm 0.04+0.00	—
A780	0.20-0.30	4.33 \pm 0.39	0.41 \pm 0.13-0.02	—
A2589	0.00-0.03	3.48 \pm 0.15	1.50 \pm 0.17-0.01	—
A2589	0.03-0.06	3.59 \pm 0.14	1.06 \pm 0.10-0.01	—
A2589	0.06-0.10	3.50 \pm 0.14	0.92 \pm 0.10-0.01	—
A2589	0.10-0.20	3.34 \pm 0.14	0.79 \pm 0.10-0.01	—
AWM7	0.00-0.03	3.44 \pm 0.05	1.12 \pm 0.06+0.01	—
AWM7	0.03-0.06	3.78 \pm 0.07	0.89 \pm 0.04+0.00	—
AWM7	0.06-0.10	3.70 \pm 0.08	0.62 \pm 0.03+0.00	—
AWM7	0.10-0.19	3.67 \pm 0.10	0.63 \pm 0.04+0.00	—
MKW3s	0.00-0.03	3.18 \pm 0.10	1.06 \pm 0.11+0.01	—
MKW3s	0.03-0.06	3.67 \pm 0.12	0.88 \pm 0.08+0.00	—
MKW3s	0.06-0.10	3.78 \pm 0.15	0.57 \pm 0.06+0.00	—
MKW3s	0.10-0.20	3.47 \pm 0.15	0.55 \pm 0.08+0.01	—
A2063	0.00-0.03	3.29 \pm 0.20	1.02 \pm 0.32-0.01	—
A2063	0.03-0.06	3.66 \pm 0.21	1.04 \pm 0.20+0.01	—
A2063	0.06-0.10	4.05 \pm 0.39	0.61 \pm 0.14-0.01	—
A3526	0.00-0.03	2.58 \pm 0.01	1.63 \pm 0.18-0.14	—
A3526	0.03-0.06	3.90 \pm 0.03	0.72 \pm 0.02+0.00	—
A3526	0.06-0.10	3.81 \pm 0.03	0.57 \pm 0.03+0.01	—
A3526	0.10-0.20	3.19 \pm 0.12	0.36 \pm 0.03+0.01	—
A2199	0.00-0.03	3.63 \pm 0.05	0.78 \pm 0.04+0.04	—
A2199	0.03-0.06	4.25 \pm 0.08	0.60 \pm 0.04-0.01	—
A2199	0.06-0.10	4.28 \pm 0.12	0.60 \pm 0.04-0.01	—
A2199	0.10-0.20	4.33 \pm 0.11	0.45 \pm 0.04-0.01	—
A2199	0.20-0.30	4.18 \pm 0.46	0.50 \pm 0.13-0.01	—
A496	0.00-0.03	3.01 \pm 0.02	0.93 \pm 0.05+0.08	—
A496	0.03-0.06	4.16 \pm 0.03	0.70 \pm 0.03+0.05	—
A496	0.06-0.10	4.72 \pm 0.05	0.61 \pm 0.04+0.01	—
A496	0.10-0.20	4.73 \pm 0.08	0.48 \pm 0.04+0.01	—
A496	0.20-0.30	3.94 \pm 0.17	0.34 \pm 0.05+0.03	—
A1644	0.03-0.06	4.47 \pm 0.43	0.76 \pm 0.22+0.04	—
A1644	0.06-0.10	4.89 \pm 0.35	0.84 \pm 0.17+0.01	—
A1644	0.10-0.20	4.95 \pm 0.30	0.64 \pm 0.11-0.00	—

cluster	r (r_{180})	kT^a (keV)	Fe (solar) from $F_{\text{FeHeK}}/F_{3.5-6}$ Best-fit ^b $\pm \Delta_{\text{stat}}^c \Delta_{\text{sys}}^d$	Fe (solar) from $F_{\text{FeHK}}/F_{3.5-6}$ Best-fit ^b $\pm \Delta_{\text{stat}}^c \Delta_{\text{sys}}^d$
A1644	0.20-0.30	4.20 \pm 0.31	0.61 \pm 0.15+0.04	—
A3562	0.00-0.03	4.62 \pm 0.24	1.37 \pm 0.17-0.01	—
A3562	0.03-0.06	4.71 \pm 0.20	0.90 \pm 0.09+0.01	—
A3562	0.06-0.10	4.85 \pm 0.20	0.75 \pm 0.09+0.02	—
A3562	0.10-0.20	4.63 \pm 0.18	0.63 \pm 0.06+0.02	—
A3562	0.20-0.30	4.49 \pm 0.34	0.52 \pm 0.14+0.02	—
A3558	0.00-0.03	5.07 \pm 0.17	0.75 \pm 0.07+0.07	—
A3558	0.03-0.06	5.88 \pm 0.17	0.64 \pm 0.07-0.01	0.83 \pm 0.19-0.01
A3558	0.06-0.10	5.87 \pm 0.16	0.50 \pm 0.06-0.01	0.49 \pm 0.13-0.01
A3558	0.10-0.20	5.29 \pm 0.11	0.46 \pm 0.04+0.02	0.53 \pm 0.14-0.07
A3558	0.20-0.30	4.77 \pm 0.16	0.45 \pm 0.05+0.07	—
A3627	0.00-0.03	5.76 \pm 0.39	0.51 \pm 0.09-0.00	—
A3627	0.03-0.06	5.74 \pm 0.29	0.49 \pm 0.07+0.01	—
A3627	0.06-0.10	6.11 \pm 0.20	0.44 \pm 0.06-0.00	—
A3627	0.10-0.20	4.97 \pm 0.17	0.52 \pm 0.06+0.06	—
A3627	0.20-0.30	4.04 \pm 0.44	0.73 \pm 0.17+0.17	—
A1795	0.00-0.03	4.21 \pm 0.05	0.86 \pm 0.04+0.11	—
A1795	0.03-0.06	5.32 \pm 0.10	0.73 \pm 0.06+0.02	0.94 \pm 0.23-0.04
A1795	0.06-0.10	5.95 \pm 0.14	0.56 \pm 0.07+0.02	0.54 \pm 0.14-0.06
A1795	0.10-0.20	6.21 \pm 0.16	0.43 \pm 0.05-0.01	0.34 \pm 0.09+0.00
A1795	0.20-0.30	6.20 \pm 0.27	0.57 \pm 0.09+0.00	—
A1795	0.30-0.50	5.72 \pm 0.62	0.35 \pm 0.10+0.03	—
A85	0.00-0.03	4.24 \pm 0.15	0.98 \pm 0.09+0.09	—
A85	0.03-0.06	5.69 \pm 0.23	0.84 \pm 0.11-0.01	—
A85	0.06-0.10	5.92 \pm 0.36	0.61 \pm 0.10-0.04	—
A85	0.10-0.20	6.11 \pm 0.32	0.52 \pm 0.08-0.02	—
A85	0.20-0.30	5.27 \pm 0.52	0.49 \pm 0.12+0.05	—
A3667	0.00-0.03	6.61 \pm 0.30	0.61 \pm 0.10-0.00	0.85 \pm 0.19-0.05
A3667	0.03-0.06	6.41 \pm 0.16	0.49 \pm 0.07+0.01	0.59 \pm 0.14-0.04
A3667	0.06-0.10	6.33 \pm 0.14	0.51 \pm 0.06+0.02	0.67 \pm 0.13-0.05
A3667	0.10-0.20	6.32 \pm 0.10	0.48 \pm 0.06+0.01	0.53 \pm 0.10-0.03
A3667	0.20-0.30	6.85 \pm 0.29	0.36 \pm 0.06-0.04	0.39 \pm 0.09+0.02
A3667	0.30-0.50	6.33 \pm 0.26	0.29 \pm 0.05+0.01	—
A426	0.00-0.03	3.79 \pm 0.01	0.78 \pm 0.02+0.13	—
A426	0.03-0.06	5.39 \pm 0.04	0.66 \pm 0.05+0.14	0.70 \pm 0.15-0.20
A426	0.06-0.10	6.28 \pm 0.07	0.54 \pm 0.06+0.06	0.56 \pm 0.10-0.06
A426	0.10-0.20	6.73 \pm 0.07	0.52 \pm 0.07-0.01	0.40 \pm 0.05+0.01
A426	0.20-0.30	6.54 \pm 0.16	0.48 \pm 0.07+0.03	0.33 \pm 0.08-0.02
A426	0.30-0.50	5.58 \pm 0.24	0.48 \pm 0.06+0.07	—
A2256	0.03-0.06	7.12 \pm 0.63	0.55 \pm 0.15-0.06	—
A2256	0.06-0.10	6.70 \pm 0.33	0.52 \pm 0.10+0.02	0.86 \pm 0.21-0.05
A2256	0.10-0.20	6.77 \pm 0.30	0.46 \pm 0.08-0.01	0.52 \pm 0.12-0.01
A2256	0.20-0.30	8.08 \pm 0.41	0.54 \pm 0.13-0.15	—
A2256	0.30-0.50	9.11 \pm 1.25	0.41 \pm 0.16-0.15	—
A3571	0.00-0.03	6.66 \pm 0.21	0.67 \pm 0.10-0.01	0.65 \pm 0.13-0.02
A3571	0.03-0.06	6.83 \pm 0.21	0.68 \pm 0.10+0.01	0.84 \pm 0.14-0.06
A3571	0.06-0.10	6.90 \pm 0.19	0.59 \pm 0.09-0.05	0.54 \pm 0.09+0.03
A3571	0.10-0.20	6.71 \pm 0.26	0.56 \pm 0.09-0.02	0.39 \pm 0.09-0.01
A3571	0.20-0.30	7.82 \pm 0.88	0.63 \pm 0.21-0.12	—
A2029	0.00-0.03	6.48 \pm 0.17	1.08 \pm 0.16+0.19	1.21 \pm 0.26-0.08
A2029	0.03-0.06	7.63 \pm 0.29	0.86 \pm 0.17+0.02	0.93 \pm 0.16-0.03
A2029	0.06-0.10	7.45 \pm 0.33	0.65 \pm 0.13+0.05	0.57 \pm 0.13-0.02
A2029	0.10-0.20	7.75 \pm 0.41	0.57 \pm 0.13+0.07	0.75 \pm 0.14-0.03
A2029	0.20-0.30	8.03 \pm 0.94	0.44 \pm 0.17-0.05	—
A1656	0.00-0.03	8.17 \pm 0.09	0.41 \pm 0.07+0.05	0.46 \pm 0.03-0.02
A1656	0.03-0.06	8.22 \pm 0.06	0.39 \pm 0.07-0.03	0.41 \pm 0.03+0.01
A1656	0.06-0.10	8.11 \pm 0.07	0.40 \pm 0.07-0.00	0.39 \pm 0.03-0.00
A1656	0.10-0.20	7.75 \pm 0.05	0.39 \pm 0.07-0.02	0.39 \pm 0.03+0.01
A1656	0.20-0.30	6.78 \pm 0.13	0.31 \pm 0.04+0.08	0.31 \pm 0.07-0.04
A1656	0.30-0.50	5.40 \pm 0.20	0.25 \pm 0.03+0.03	—
A3266	0.00-0.03	7.59 \pm 0.44	0.60 \pm 0.14+0.06	0.79 \pm 0.17-0.04

cluster	r (r_{180})	kT^a (keV)	Fe (solar) from $F_{\text{FeHeK}}/F_{3.5-6}$ Best-fit ^b $\pm \Delta_{\text{stat}}^c \Delta_{\text{sys}}^d$	Fe (solar) from $F_{\text{FeHK}}/F_{3.5-6}$ Best-fit ^b $\pm \Delta_{\text{stat}}^c \Delta_{\text{sys}}^d$
A3266	0.03-0.06	8.29 \pm 0.39	0.58 \pm 0.13-0.02	0.55 \pm 0.11-0.00
A3266	0.06-0.10	8.21 \pm 0.31	0.49 \pm 0.10+0.00	0.38 \pm 0.09-0.01
A3266	0.10-0.20	8.09 \pm 0.21	0.46 \pm 0.09-0.02	0.46 \pm 0.06+0.01
A3266	0.20-0.30	6.86 \pm 0.30	0.33 \pm 0.07+0.03	0.42 \pm 0.12-0.00
A3266	0.30-0.50	6.29 \pm 0.47	0.48 \pm 0.12+0.13	—
A754	0.03-0.06	8.93 \pm 0.60	0.45 \pm 0.12+0.03	0.62 \pm 0.13-0.01
A754	0.06-0.10	8.85 \pm 0.42	0.58 \pm 0.13-0.02	0.36 \pm 0.08+0.01
A754	0.10-0.20	9.66 \pm 0.38	0.52 \pm 0.11-0.06	0.47 \pm 0.06+0.01
A754	0.20-0.30	10.04 \pm 1.67	0.38 \pm 0.16-0.04	0.54 \pm 0.12-0.01

^aBest-fit ICM temperature with 1σ statistical error derived from the 1T model fits

^bBest-fit Fe abundance using the ICM temperature derived from the 1T model fits

^c1 σ statistical error, considering a 10 % systematic uncertainty in the ICM temperature derived from the 1T model.

^d Difference in the derived Fe abundances using the best-fit multi-T model and the 1T model